Optical measurements of structure and orientation in sheared carbon-nanotube suspensions

E. K. Hobbie,[a] H. Wang, H. Kim,[b] and C. C. Han
National Institute of Standards and Technology, Gaithersburg, Maryland 20899

E. A. Grulke
Advanced Carbon Materials Center, University of Kentucky, Lexington, Kentucky 40506

J. Obrzut
National Institute of Technology, Gaithersburg, Maryland 20899

(Received 2 October 2002; accepted 1 November 2002)

We describe an optical metrology for measuring shear-induced structure and orientation in dilute dispersions of multiwalled carbon nanotubes. Small-angle polarized light scattering and optical microscopy are combined *in situ* to quantify the structural anisotropy of multiwalled carbon nanotubes in semidilute, surfactant-stabilized aqueous suspensions under simple shear flow. Measurements performed as a function of the applied shear rate are used to demonstrate the capabilities and limitations of the experimental technique, which should be suitable for probing the shear response of polymer-nanotube melts and solutions. © *2003 American Institute of Physics.* [DOI: 10.1063/1.1540722]

I. INTRODUCTION

Nanocomposite materials made out of polymers and carbon nanotubes offer the promise of plastic composites with enhanced structural, electrical, thermal, and optical properties.[1–11] As inorganic filler in an organic polymer matrix, carbon nanotubes are structurally unique in that the tube diameter can be the same order of magnitude as the radius of gyration of the polymer,[1] yet the aspect ratio of the tubes can be exceptionally large[12] and the tubes themselves can exhibit extreme strength.[13] In addition to the resolution of fundamental issues concerning the fractionation, functionalization, and dispersion of multi- and single-walled carbon nanotubes in a broad array of organic solvents and polymer matrices,[14,15] efficient bulk processing of nanotube/polymer composites will depend in part on a detailed understanding of the response of carbon nanotube suspensions and melts to simple steady shear flow. In this article, we describe an optical metrology for measuring shear-induced structure and orientation in semidilute dispersions of multiwalled carbon nanotubes. Small-angle polarized light scattering and optical microscopy are combined *in situ* to quantify the structural anisotropy that develops in surfactant-stabilized aqueous nanotube suspensions under steady shear flow. The method should be suitable for optically probing the shear response of polymer/nanotube melts and solutions in both the dilute and semidilute limit.

II. MATERIALS AND METHODS

The multiwalled carbon nanotubes (MWNTs) used in this study were produced via a chemical vapor deposition process.[16] The reactor is an open quartz tube at atmospheric pressure. Controlled flows of a catalyst, a carbon source, an inert gas, and hydrogen are used to grow the nanotubes on the reactor surfaces. In this case, the catalyst precursor was ferrocene, the carbon source was xylene, and a 10:1 argon:hydrogen ratio was used. Argon was used to purge oxygen from the reactor while heating it to the synthesis temperature (700–800 °C). A ferrocene–xylene solution was fed into the reactor over the 2 h reaction period. Control of the reactor conditions results in nanotube deposition in the hot zone of the furnace. Iron nanoparticles are formed on the reactor surfaces and catalyze the growth of the tubes. These nanoparticles probably catalyze the decomposition of the carbon source as they synthesize the tubes. The tubes grow in ''mats'' of locally uniform height that can be removed by mechanical means and have diameter and height distributions that can be varied by changing the reactor conditions. A scanning-electron microscope (SEM) image of typical tubes used in the measurements is shown in Fig. 1. The actual persistence length (between 1 and 10 μm) appears to be limited by the presence of bends along the tube backbone, and the cartoon in the lower left corner of Fig. 1 depicts simple geometries that model the effective shape of the semiflexible tubes. Based on SEM measurements, the tubes have a mean diameter $d \approx 50$ nm with $M_w/M_n = 1.10$, and based on optical microscopy measurements (200× magnification, after aqueous suspension), the tubes have a mean length $L \approx 12\ \mu$m with $M_w/M_n = 2.6$.

To prepare aqueous colloidal suspensions from the tubes, we dissolved 3 g of the surfactant phenoxy–ethyleneoxy in 100 g of water and mechanically mixed in 0.24 g of MWNTs. The solution was then sonicated for 30 min, and large aggregates and impurities were allowed to settle out of the final suspension. The final suspensions are semidilute, with $nL^3 \approx 75$ and $nL^2 d \approx 0.32$, where n is the number of

[a]Author to whom correspondence should be addressed; electronic mail: erik.hobbie@nist.gov
[b]Also with Dept. of Chemistry, Kyunghee University, Yongin, Kyungkido, Korea 449-701.

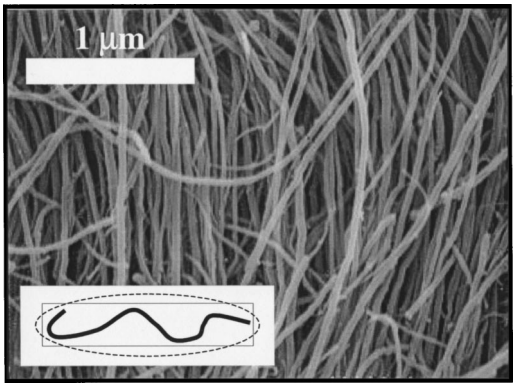

FIG. 1. SEM of typical MWNTs used to make suspensions, where the white scale bar is 1 μm. The tubes are semiflexible, with a persistence length between 1 and 10 μm. The cartoon depicts simple geometrical models of the effective shape of the nanotubes.

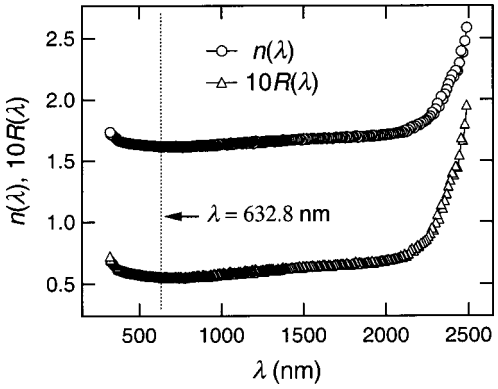

FIG. 2. Reflectance spectrum $[R(\lambda)$, multiplied by 10] and the estimated magnitude of the complex index of refraction $[n(\lambda)]$ deduced from $R(\lambda)$ over the interval 300 nm$<\lambda<$2500 nm. In determining $n(\lambda)$, the phase angle of the complex reflectance has been neglected. In the vicinity of $\lambda=632.8$ nm, the estimated magnitude of the index of refraction is 1.6.

tubes per unit volume. The suspensions prepared in this manner were stable over the course of many months. Vigorous shaking and sonication for 30 min were sufficient to redisperse any tubes that eventually settled out of solution over an extended period. This slow sedimentation likely reflects gradual gravitational settling of the larger tubes, but entropic phase-separation (depletion) effects associated with micelles of excess surfactant in solution might play a role as well. When we prepare bimodal suspensions containing 0.12% MWNT (by mass) and 20 nm diam colloidal silica (0.20 volume fraction), for example, the tubes completely phase separate out of solution over the course of 1 day.

Any optical probe of a nanotube suspension will depend on the optical properties of the tubes, which appear black in bulk quantities due to absorption in the visible spectrum (the index of refraction, n, has a small but significant imaginary component). Suspensions prepared at 0.24% MWNT by mass appear black in the test tube but are a transparent gray when confined within the 200–400 μm gap of the optical shear cell. To obtain an estimate of the modulus $|n|$ as a function of wavelength λ, we prepared amorphous dry films of the MWNTs (with surfactant) on quartz substrates. These films were sufficiently thick as to appear completely black and opaque. The reflectance at normal incidence, $R(\lambda)=|(1-n)/(1+n)|^2$, was then measured over the interval 300 nm$<\lambda<$2500 nm (Fig. 2) with a Perkin Elmer Lambda 9 ultraviolet/visible/near infrared spectrophotometer.[17] Note that R is the square amplitude of a complex reflectivity, $\tilde{R}=\sqrt{R}e^{i\beta}$, and the real and imaginary parts of n can thus be expressed in terms of $\sqrt{R}$ and β, with $|n|$ depending on both. In principle, these two quantities are related via the Kramers–Kronig relations,[18] but upturns in $R(\lambda)$ at both ends of the measured interval (Fig. 2) make such a computation difficult. The symmetry of the Kramers–Kronig relations, however, suggests that $\beta(\lambda)$ should be small when $R(\lambda)$ remains constant over a sufficiently broad interval of λ. From the shape of $R(\lambda)$ in the vicinity of $\lambda=632.8$ nm, we expect the imaginary part of n to be smaller than the real part, and neglecting it provides the leading-order estimate $|n|\approx 1.6$ at $\lambda=632.8$ nm. The small magnitude of the imaginary part and the approximate modulus are consistent with the measured dielectric spectra of other fullerenes,[19] and we expect limitations on the first Born approximation to be qualitatively similar to those encountered in light scattering from aqueous suspensions of polymeric colloids, which must be kept sufficiently dilute to ensure a simple interpretation of the scattering measurement.[20]

The light-scattering/microscopy instrument, capable of both real- and reciprocal-space measurements in the flow/vorticity plane, was designed and constructed for conducting optical measurements of complex fluids under simple shear flow.[21] The geometry of the experiment is show in Fig. 3. The flow direction is along the x axis, the gradient direction is along the y axis, and the vorticity direction is along the z axis. The sample is placed between two quartz plates, the upper of which rotates at a controlled angular speed. The gap between the plates varied between 200 and 400 μm, and the angular speed was controlled to set the shear rate ($\dot{\gamma}=\partial v_x/\partial y$) at a point of observation 2 cm from the center of the 4 cm (radius) plates, where the local flow is simple shear. The Reynolds number is $\mathrm{Re}\approx\dot{\gamma}\ell^2\rho/\eta$, where ℓ is the width of the gap, and ρ and η are the density and viscosity, respectively, of water at ambient temperature ($T=25\,^\circ$C, where all of the measurements described here were performed). At the highest shear rate used in the present study ($\dot{\gamma}=50\,\mathrm{s}^{-1}$), we estimate that Re is of order 2. Since all potential suspending fluids of interest for future study are more viscous than water, inertial effects are assumed to be negligible.

A beam of polarized monochromatic light from a 15 mW

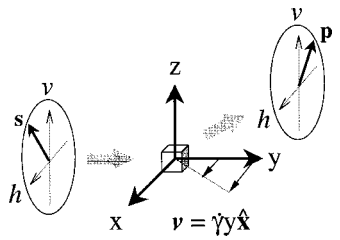

FIG. 3. The geometry of the shear light-scattering experiment, where **s** is the polarization of the incident beam and **p** is the polarization of the analyzer. The flow h direction is along the x axis, the gradient direction is along the y axis, and the vorticity (v) direction is along the z axis.

He–Ne laser ($\lambda = 632.8$ nm) is directed through the sample. After passing through the analyzing polarizer, the image of the scattered light in the angular range 4°–27° with respect to the incident beam, corresponding to wave vector q values ranging from 0.58 to 4.9 μm^{-1}, is focused onto a thermoelectrically cooled two-dimensional charge-coupled-device (CCD) detector using a pair of spherical condensers, and the array of data from the 256×256 pixel CCD camera is then transferred to a personal computer. The polarization of the incident beam is denoted **s** and the polarization of the analyzer is denoted **p**. In this study we measure the four configurations hh ($\mathbf{s}=\hat{\mathbf{x}},\mathbf{p}=\hat{\mathbf{x}}$), vv ($\mathbf{s}=\hat{\mathbf{z}},\mathbf{p}=\hat{\mathbf{z}}$), hv ($\mathbf{s}=\hat{\mathbf{x}},\mathbf{p}=\hat{\mathbf{z}}$), and vh ($\mathbf{s}=\hat{\mathbf{z}},\mathbf{p}=\hat{\mathbf{x}}$), where $\hat{\mathbf{x}}$ and $\hat{\mathbf{z}}$ define the flow and vorticity directions, respectively. The microscope image is collected with a different CCD camera (Dage MTI, model 72), recorded onto a super-VHS tape, and digitized using a frame grabber from Data Translation (DT 3851). A strobe flash synchronized with the video frame acquisition provides sharp images at high shear rates.

III. RESULTS

Figure 4 shows a light-scattering/micrograph pair for a quiescent MWNT suspension prepared at 0.24% MWNT by mass, where the width of the micrograph is 100 μm. The quiescent suspension is isotropic, and the anisotropy of the hh and vv patterns are related by a 90° rotation about the gradient (y) direction. The hv and vh patterns are nearly symmetric four-lobed shapes with scattering maxima oriented at odd integer multiples of 45°. The tubes appear as faint, dark, anisotropic shapes in the optical micrographs, with the largest tubes being darkest and most distinct. Due to the weakness of the real-space optical signal, spurious anisotropy along the flow direction associated with the video imaging technique is apparent in the micrograph, and this background will be removed from the real-space data. Figure 5 shows a light-scattering/micrograph pair for the suspension depicted in Fig. 4 at $\dot{\gamma} = 50\,s^{-1}$. Broad orientation of the tubes along the flow direction is evident in the anisotropy of the hh and vv patterns (relative to that in Fig. 4), and in the change in orientation of the lobes in the hv and vh patterns. The mean orientation of the tubes is also evident in the micrograph.

To infer information about the orientation of the nanotubes from the hh and vv light-scattering patterns, we consider projections of these structure factors along the flow and vorticity directions, as shown in Fig. 6 for a 0.24% by mass aqueous MWNT suspension at a shear rate of 0.1 s^{-1}. At this low shear rate, the suspension is essentially isotropic, and the anisotropy is analogous to that depicted in Fig. 4. In the Appendix, we derive general expressions for the measured structure factors within the first Born approximation. There are four characteristic length scales contained in the hh and vv scattering patterns: ξ_{hx}, ξ_{hz}, ξ_{vx}, and ξ_{vz}. To extract these, we fit the data to $S(q_i) \approx S(0)\exp(-\xi_i^2 q_i^2/2)$ in the low-q limit,[22] and Fig. 7 shows the four length scales as a function of $\dot{\gamma}$ for a 0.24% by mass MWNT suspension. For the hh pattern, orientation of the tubes along the flow direction leads to a decrease in ξ_{hz}, while ξ_{hx} remains saturated at around 0.8 μm (although the tubes are on the order of 10 μm in length, objects of this dimension will tend to scatter at angles near the beam stop). For the vv pattern, orientation of the tubes along the direction of flow is apparent as a shear-induced increase in ξ_{vx} and a shear-induced decrease in ξ_{vz}.

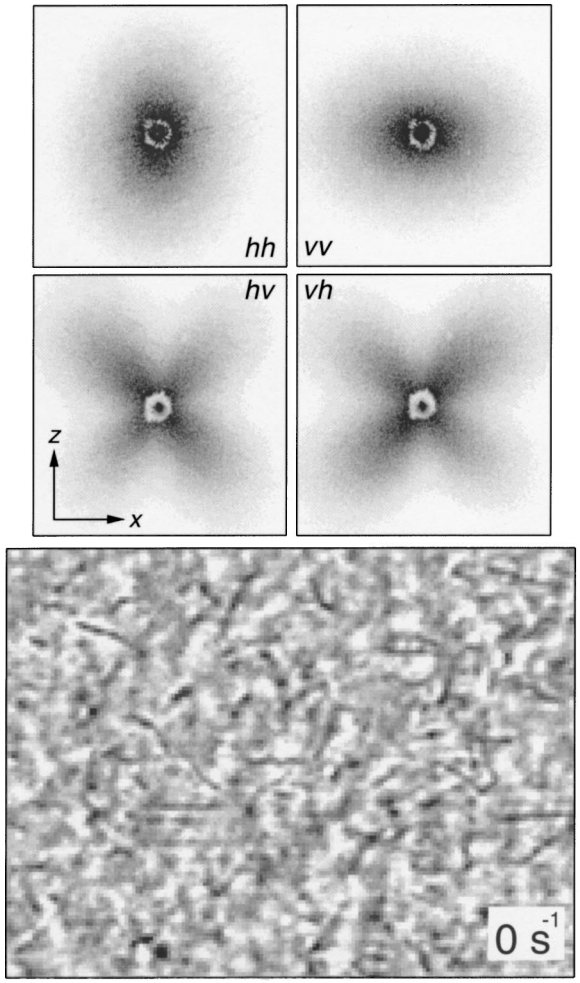

FIG. 4. Light-scattering/micrograph pair for a quiescent aqueous suspension prepared at 0.24% MWNT by mass, where the measurements are taken in the flow-vorticity (x–z) plane. The scattering intensity depends on the relative configuration of the two polarizations **s** and **p**, and in this study we measure the four configurations hh ($\mathbf{s}=\hat{\mathbf{x}},\mathbf{p}=\hat{\mathbf{x}}$), vv ($\mathbf{s}=\hat{\mathbf{z}},\mathbf{p}=\hat{\mathbf{z}}$), hv ($\mathbf{s}=\hat{\mathbf{x}},\mathbf{p}=\hat{\mathbf{z}}$), and vh ($\mathbf{s}=\hat{\mathbf{z}},\mathbf{p}=\hat{\mathbf{x}}$), where $\hat{\mathbf{x}}$ and $\hat{\mathbf{z}}$ define the flow and vorticity directions, respectively. The width of the micrograph is 100 μm and the light-scattering pattern subtends an angle of ±27°.

Information about the mean orientation of the tubes is also contained in the angles locating the lobes of maximum intensity in $S_{hv}(\mathbf{q})$ and $S_{vh}(\mathbf{q})$, which we denote ϕ. In the Appendix, we note that one can derive the simple relation $\phi = \pm(\pi/2 - \theta_m) \pm n\pi (n = 0,1,2,...)$, where the angle θ_m locates the maximum in the effective probability distribution function $p(\theta)\sin^2\theta\cos^2\theta$. Here, $p(\theta)$ is the measured tilt-angle distribution function, where the tilt angle is defined as the angle between the flow (x) direction and the projection of the tube orientation axis into the x–z plane. For an isotropic system [$p(\theta) = \text{constant}$], the maxima thus occur at odd multiples of 45°, in agreement with the behavior depicted in the vh and hv light-scattering patterns shown in Fig. 4. Figure 8 shows the angle θ_m inferred from the hv and vh light-scattering data as a function of $\dot{\gamma}$, where the inset shows the

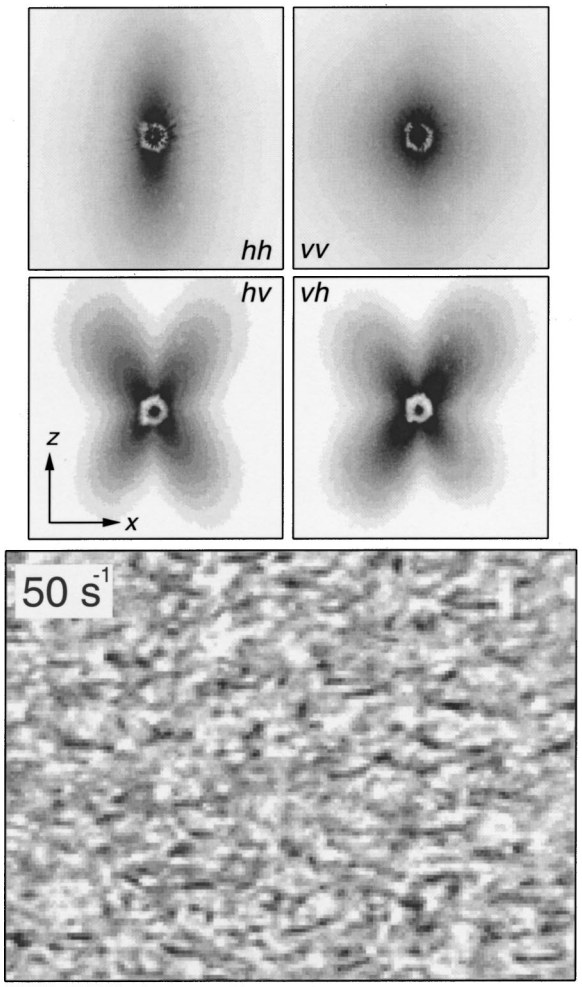

FIG. 5. Light-scattering/micrograph pair for the suspension in Fig. 4 at a shear rate of 50 s^{-1}. Orientation of the tubes along the flow direction is evident in the anisotropy of the hh and vv patterns, and in the orientation of the intensity lobes in the hv and vh patterns. The mean orientation of the tubes is also evident in the micrograph. The geometry is the same as that in Fig. 4.

vh pattern at $\dot{\gamma}=0.1\,s^{-1}$, with the angles θ_m and ϕ as indicated. As the tubes orient with the flow direction, the scattering lobes thus rotate toward the vorticity axis.

For the real-space data provided by the optical micrographs, Fig. 9 shows how the distribution function $p(\theta)$ is extracted from these images. Micrographs (top) are first thresholded into binary images (bottom), and shapes with an area above a lower cutoff of 4 μm^2 (outlined) are then used to determine the effective two-dimensional orientation, defined as the axis that yields the smallest moment of inertia. In Fig. 9, the sample on the left is at rest, while $\dot{\gamma}=50\,s^{-1}$ for that on the right. The width of each image is 70 μm. As mentioned above, correlated pixelation associated with the video imaging technique leads to weak spurious anisotropy along the flow direction. Figure 10(a) shows the tilt-angle distribution functions $p(\theta)$ for the data depicted in Fig. 9. The histograms have been made symmetric with respect to $\theta=90°$ to eliminate slight residual anisotropy in the ensembles, which contain on the order of 4000 individual shapes. Note that the uncorrected quiescent data are weakly peaked along the flow direction, and this background is subtracted from the raw data to get the corrected histograms. Based on these corrected distributions, the effective probability distributions relevant to the hv and vh scattering patterns, $p(\theta)\sin^2\theta\cos^2\theta$, are easily computed and are shown in Fig. 10(b). The dark triangles indicate the locations of the maxima suggested by the hv and vh light-scattering patterns.

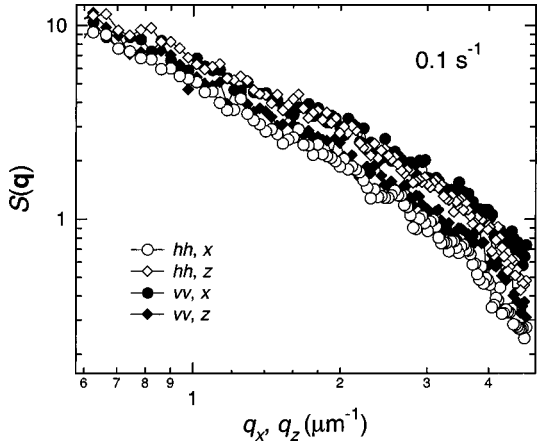

FIG. 6. The low-q structure factors $S_{hh}(\mathbf{q})$ and $S_{vv}(\mathbf{q})$ projected onto the flow (x) and vorticity (z) directions for a 0.24% by mass aqueous MWNT suspension at a shear rate of 0.1 s^{-1}. At this low shear rate, the suspension is more or less isotropic, and the anisotropy in the scattering is analogous to that depicted in Fig. 4.

IV. DISCUSSION

Because most polymer melts have an index of refraction on the order of 1.5–1.6, we expect this approach to be well suited to measuring the shear response of MWNTs dispersed in a polymer melt or solution, as long as the tubes are sufficiently dilute or the probed volume is sufficiently thin. The viscoelasticity of a polymer melt or solution should allow us to access a regime of higher shear stress, and we expect that elastic stresses present in such fluids might influence the orientation of the tubes, as well as their aggregation and dispersion behavior. An understanding of how shear flow orients and disperses carbon nanotubes in a polymer melt or solution

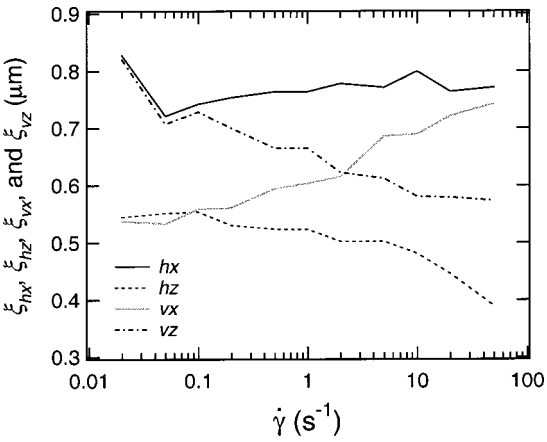

FIG. 7. The four characteristic length scales determined from the hh and vv light-scattering patterns (ξ_{hx}, ξ_{hz}, ξ_{vx}, and ξ_{vz}) as a function of shear rate for a 0.24% by mass MWNT suspension. A discussion of the trends suggested by the data is given.

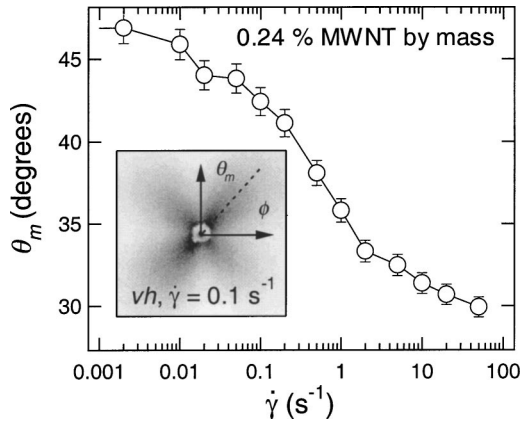

FIG. 8. The angle θ_m as a function of shear rate for a 0.24% by mass MWNT suspension, where $\theta_m = 45°$ corresponds to an isotropic configuration. The inset shows the vh light-scattering pattern at $\dot{\gamma} = 0.1\ s^{-1}$, with the angles θ_m and ϕ as indicated.

might contribute, for example, to the understanding and elimination of residual surface effects associated with the injection molding or flow coating of nanotube composite parts, and it is hoped that the experimental technique described here might prove to be an efficient and useful means of inferring such information. A detailed study of the shear response of MWNTs dispersed in polymeric fluids will be presented elsewhere.

Although the aim of the current article is to describe an optical metrology for probing structure and orientation in MWNT suspensions, we note that both the observed orientation of the tubes along the flow direction and the apparent broadness of the distribution are a reflection of the fundamental nature of dilute and semidilute fiber suspensions under simple shear flow. By choosing a focal plane close to the stationary bottom wall, we can observe individual tubes as they traverse the field of view at high shear rates. These

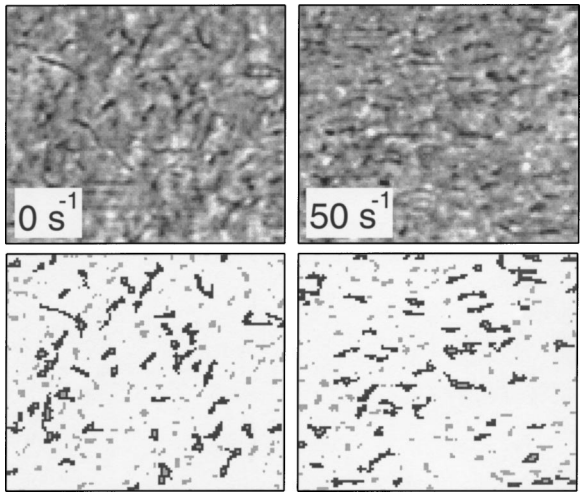

FIG. 9. Micrographs (top) are thresholded into binary images (bottom), and shapes with an area above a lower cutoff (outlined) are used to map out the orientation of the tubes. The orientation of a region is defined as the axis that yields the smallest moment of inertia. The sample on the left is at rest (Fig. 4), while that on the right is under simple shear flow with $\dot{\gamma} = 50\ s^{-1}$ (Fig. 5). The width of each image is 70 μm. Correlated pixelation associated with the video imaging technique leads to weak spurious anisotropy along the flow direction.

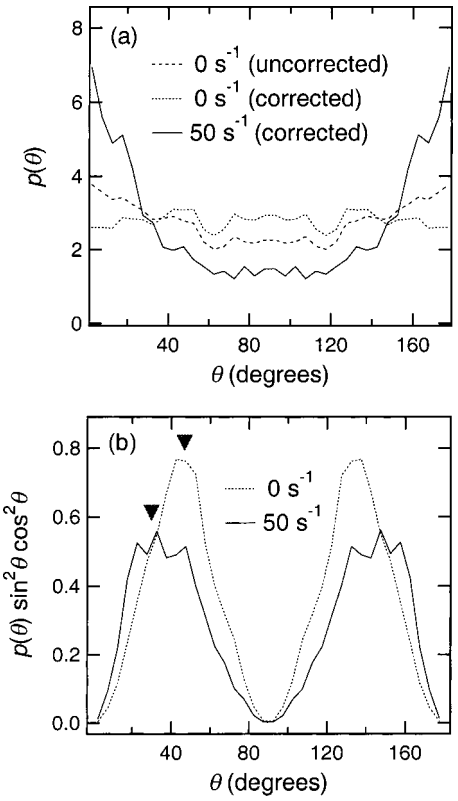

FIG. 10. (a) Tilt angle distribution functions, $p(\theta)$, for the data depicted in Fig. 9. The histograms have been made symmetric with respect to $\theta = 90°$ to eliminate very slight residual anisotropy in the ensembles. The uncorrected quiescent data are weakly peaked along the flow direction. (b) Effective probability distributions (relevant for the hv and vh scattering patterns) based on the real-space distributions shown in (a). The dark triangles indicate the location of the maxima suggested by the hv and vh light-scattering patterns.

observations suggest that some of the tubes rotate about the vorticity axis, as they appear to rock back and forth in the $x-z$ plane. They also suggest that the tubes can undergo large deformations during shear flow, while quiescent observations suggest that the tubes can exhibit modest deformation as a consequence of thermal (Brownian) fluctuations, consistent with their semiflexible nature.

A theoretical treatment of an isolated rod-like particle in simple shear flow gives the so-called Jeffery orbit in which the particle undergoes an oblate precession about the vorticity axis.[23,24] These orbits are characterized by a constant C describing the shape of the trajectory, where $C = 0$ corresponds to perfect alignment along the z axis and $C = \infty$ corresponds to circular rotation within the $x-y$ plane. This constant is not uniquely determined by the shear rate but depends on the initial conditions of the particle.[24] The particle aspect ratio, which for MWNTs is potentially quite large, is also an important factor, and we note that for very long slender rods the majority of the orbit is predicted to be spent aligned with the flow direction.[25] The influence of fiber flexibility on the particle orbit has also been measured and calculated,[26] and the role that hydrodynamic tube–tube interactions play in determining the steady-state distribution of orbit constants in dilute and semidilute fiber suspensions has also been calculated and measured.[27,28] Our data suggest that

the distribution in these semidilute suspensions of Brownian nanofibers is broadly peaked around $C=\infty$. Note that this analogy is somewhat qualitative, as we have not actually measured the three-dimensional orbits of individual tubes. It is consistent with measurements of particle motion in dilute rod-like and fiber suspensions under shear, however, which also suggest a distribution that appears broadly peaked around the flow direction when viewed in the $x-z$ plane.[27–29]

APPENDIX

A quantitative description of the scattering of polarized light from a collection of optically anisotropic objects follows from the analysis of Stein and Wilson.[30] We assume that the tubes have cylindrical symmetry,[31] where $(\alpha_{\parallel})_j$ and $(\alpha_{\perp})_j$ denote the polarizability of the jth scattering element along directions parallel ($\parallel$) and perpendicular ($\perp$) to the local symmetry axis $\hat{\mathbf{n}}_j$. The geometry of the scattering experiment is shown in Fig. 3, where $\mathbf{s}$ is the polarization of the incident beam and $\mathbf{p}$ is the polarization of the analyzer. Within the first Born approximation, the intensity of scattered light is[30]

$$S(\mathbf{q}) \propto \sum_k \sum_j (\mathbf{m}_k \cdot \mathbf{p})(\mathbf{m}_j \cdot \mathbf{p}) e^{i\mathbf{q}\cdot\mathbf{r}_{kj}}, \tag{A1}$$

where the indices j and k run over all of the scattering elements of the system. The field induced in the jth element $\mathbf{m}_j$ is proportional to $\delta_j(\mathbf{s}\cdot\hat{\mathbf{n}}_j)\hat{\mathbf{n}}_j + (\alpha_j - \frac{1}{3}\delta_j)\mathbf{s}$, where $\alpha_j = (\alpha_{\parallel} + 2\alpha_{\perp})_j/3$ and $\delta_j = (\alpha_{\parallel} - \alpha_{\perp})_j$ are the magnitude and anisotropy, respectively, of the polarizability of the jth scattering element.[30] The scattering intensity [Eq. (A1)] depends on the relative configuration of the two polarizations $\mathbf{s}$ and $\mathbf{p}$, and in this study we measure hh ($\mathbf{s}=\hat{\mathbf{x}}, \mathbf{p}=\hat{\mathbf{x}}$), vv ($\mathbf{s}=\hat{\mathbf{z}}, \mathbf{p}=\hat{\mathbf{z}}$), hv ($\mathbf{s}=\hat{\mathbf{x}}, \mathbf{p}=\hat{\mathbf{z}}$), and vh ($\mathbf{s}=\hat{\mathbf{z}}, \mathbf{p}=\hat{\mathbf{x}}$) scattering, where $\hat{\mathbf{x}}$ and $\hat{\mathbf{z}}$ are the flow and vorticity directions, respectively. Formally, the structure factors are

$$S_{\alpha\beta}(\mathbf{q}) \propto \left| \sum_k \hat{\mathbf{x}}_\alpha \cdot \mathbf{F}_k(\mathbf{q}) \cdot \hat{\mathbf{x}}_\beta e^{i\mathbf{q}\cdot\mathbf{r}_k} \right|^2. \tag{A2}$$

The index k in Eq. (A2) now runs over all of the tubes in the scattering volume, with the vector $\mathbf{r}_k$ locating the centroid of the kth tube, and with the form-amplitude tensor given by

$$\mathbf{F}_k(\mathbf{q}) = N_k^{-1} \sum_{j=1}^{N_k} [\delta(\hat{\mathbf{n}}_{kj}\hat{\mathbf{n}}_{kj}) + (\alpha - \tfrac{1}{3}\delta)\mathbf{1}] e^{i\mathbf{q}\cdot\mathbf{r}_{kj}}. \tag{A3}$$

The index j in Eq. (A3) runs over the N_k ''segments'', or steps $\hat{\mathbf{n}}_{kj}$, comprising the backbone of the kth tube, and $\mathbf{1}$ is the identity tensor. The vector $\mathbf{r}_{kj}$ locates the jth element of the kth tube with respect to its center $\mathbf{r}_k$. It is convenient to recast Eq. (A3) in terms of the mean orientation of the kth tube $\hat{\mathbf{n}}_k$, defined as the eigenvector with the smallest eigenvalue of the inertia tensor

$$\mathbf{I}_k = N_k^{-1} \sum_{j=1}^{N_k} [(\mathbf{r}_{kj}\cdot\mathbf{r}_{kj})\mathbf{1} - \mathbf{r}_{kj}\mathbf{r}_{kj}], \tag{A4}$$

where $\Sigma_j \mathbf{r}_{kj} = 0$. Defining the local deviation $\Delta_{kj} = \hat{\mathbf{n}}_{kj} - \hat{\mathbf{n}}_k$ and neglecting terms in Eq. (A3) that are linear and quadratic in Δ_{kj}, the four measured structure factors are

$$S_{hh}(\mathbf{q}) \propto \left| \sum_k [\delta(\hat{\mathbf{n}}_k\cdot\hat{\mathbf{x}})^2 + (\alpha - \tfrac{1}{3}\delta)] e^{i\mathbf{q}\cdot\mathbf{r}_k} f_k(\mathbf{q}) \right|^2, \tag{A5}$$

$$S_{vv}(\mathbf{q}) \propto \left| \sum_k [\delta(\hat{\mathbf{n}}_k\cdot\hat{\mathbf{z}})^2 + (\alpha - \tfrac{1}{3}\delta)] e^{i\mathbf{q}\cdot\mathbf{r}_k} f_k(\mathbf{q}) \right|^2, \tag{A6}$$

and

$$S_{vh}(\mathbf{q}) = S_{hv}(\mathbf{q}) \propto \left| \sum_k \delta(\hat{\mathbf{n}}_k\cdot\hat{\mathbf{x}})(\hat{\mathbf{n}}_k\cdot\hat{\mathbf{z}}) e^{i\mathbf{q}\cdot\mathbf{r}_k} f_k(\mathbf{q}) \right|^2, \tag{A7}$$

where the index k runs over the tubes and the form amplitude, $f_k(\mathbf{q}) \propto \Sigma_j e^{i\mathbf{q}\cdot\mathbf{r}_{kj}}$, contains information about their effective shape. We assume that α and δ are homogeneous throughout the sample. The neglected terms are of order $\langle\Delta_{kj}\rangle = \hat{\mathbf{n}}'_k - \hat{\mathbf{n}}_k$, where $\hat{\mathbf{n}}'_k = N_k^{-1}\Sigma_j \hat{\mathbf{n}}_{kj}$ is the end-to-end vector of the kth tube. For most of the tubes this difference will be small, and higher order terms can thus be neglected.

To proceed further requires a relative magnitude for α and δ and a specific model for $f_k(\mathbf{q})$. Within the scope of the present work, a physical understanding is not difficult to achieve. For the hh and vv scattering intensities, the scattering amplitude contains an additive term proportional to $(\hat{\mathbf{n}}_k \cdot \hat{\mathbf{x}})^2$ or $(\hat{\mathbf{n}}_k\cdot\hat{\mathbf{z}})^2$, respectively, implying that $S_{hh}(\mathbf{q})$ is more sensitive to tube alignment along the flow direction, while $S_{vv}(\mathbf{q})$ is more sensitive to alignment along the vorticity direction. The length scales ξ_{hx}, ξ_{hz}, ξ_{vx}, and ξ_{vz} deduced from these structure factors are thus coherence lengths containing information about the director distribution and the shape of the individual tubes. For example, if the tubes were all ideally straight and perfectly aligned along $\hat{\mathbf{x}}$, then the hh and vv patterns would differ only in overall intensity, with ξ_{hx} (ξ_{vx}) corresponding to the apparent mean tube length and ξ_{hz} (ξ_{vz}) corresponding to the mean tube diameter, the difference in intensity simply reflecting the anisotropy in $\alpha_{\parallel}$ and $\alpha_{\perp}$.

The nature of the vh and hv patterns is also easy to understand. In this case, the scattering amplitude is proportional to $(\hat{\mathbf{n}}_k\cdot\hat{\mathbf{x}})(\hat{\mathbf{n}}_k\cdot\hat{\mathbf{z}})$, which is zero for tubes aligned with either the flow or vorticity directions. Making the decomposition $q_x = q\cos\phi$ and $q_z = q\sin\phi$, an isotropic suspension will then exhibit lobes of maximum scattering intensity when ϕ is equal to odd multiples of $\pi/4$ (see Fig. 4). Modeling the projection of the tubes into the flow-vorticity plane as a two-dimensional (2D) collection of length-polydisperse, high-aspect-ratio rectangles in the $x-z$ plane (with the tilt angle θ defined as the angle between $\hat{\mathbf{x}}$ and the $x-z$ projected director), one can derive the simple relation $\phi = \pm(\pi/2 - \theta_m) \pm n\pi$ ($n=0,1,2,...$) giving the angular locations of the maximum intensity lobes, where the angle θ_m locates the maximum in the effective probability distribution function $p(\theta)\sin^2\theta\cos^2\theta$. Here, $p(\theta)$ is the tilt-angle distribution function discussed in the article. As the tubes orient with the flow direction, the lobes thus move away from $\pi/4$ toward the vorticity axis, reflecting the inverted nature of the response in q space.

To infer a measure of the physical tube dimensions from the light-scattering data requires a model for their shape and a quantitative knowledge of the dielectric anisotropy. We note that if the MWNTs could be straightened out and per-

fectly aligned, then the technique described here would provide a direct measure of the optical anisotropy. Assuming $\alpha_{\parallel} \gg \alpha_{\perp}$, a low-$q$ expansion of the simple 2D model mentioned above gives

$$\xi_{hx}^2 \approx \tfrac{1}{3}\{w^2\langle \cos^4\theta \sin^2\theta\rangle + L_{\mathrm{eff}}^2\langle \cos^6\theta\rangle\}/\langle \cos^4\theta\rangle, \quad \text{(A8)}$$

$$\xi_{hz}^2 \approx \tfrac{1}{3}\{w^2\langle \cos^6\theta\rangle + L_{\mathrm{eff}}^2\langle \cos^4\theta \sin^2\theta\rangle\}/\langle \cos^4\theta\rangle, \quad \text{(A9)}$$

$$\xi_{vx}^2 \approx \tfrac{1}{3}(w^2\langle \sin^6\theta\rangle + L_{\mathrm{eff}}^2\langle \sin^4\theta \cos^2\theta\rangle)/\langle \sin^4\theta\rangle, \quad \text{(A10)}$$

and

$$\xi_{vz}^2 \approx \tfrac{1}{3}(w^2\langle \sin^4\theta \cos^2\theta\rangle + L_{\mathrm{eff}}^2\langle \sin^6\theta\rangle)/\langle \sin^4\theta\rangle, \quad \text{(A11)}$$

where the brackets denote an average over $p(\theta)$. For the lowest shear rate shown in Fig. 7, the above equations give $w \approx 850$ nm and $L_{\mathrm{eff}} \approx 1.5\,\mu$m, where these length scales represent apparent values of the mean tube dimensions projected into the $x-z$ plane. In principle, the smallness of L_{eff} (compared to $L \approx 12\,\mu$m) might be attributed to both a low-q cutoff arising from the beam stop and the small projected length (in the $x-z$ plane) of tubes whose $\hat{\mathbf{n}}_k$ has a large out-of-plane (y) component. The magnitude of w (compared to the tube width suggested by SEM) might be attributed to the semiflexible nature of the tubes, which even in quiescence contain internal ''bends'' reflecting a finite persistence length.[32] A more accurate 3D model, however, is clearly needed. When the above ''bare'' values of the tube dimensions and the measured $p(\theta)$ are combined with Eqs. (A8)–(A11), for example, they predict the correct sign of the trends observed in each of the four length scales with increasing $\dot{\gamma}$ (see Fig. 7), but the magnitude of the change is grossly underestimated.

[1] T. W. Ebbesen, *Carbon Nanotubes* (Chemical Rubber Corp., Boca Raton, FL, 1997).
[2] M. M. J. Treacy, T. W. Ebbesen, and J. M. Gibson, Nature (London) **381**, 678 (1996).
[3] P. Poncharal *et al.*, Science **283**, 1513 (1999).
[4] S. J. Tans, A. R. M. Verschueren, and C. Dekker, Nature (London) **393**, 49 (1998).
[5] H. Dai, E. W. Wong, and C. M. Lieber, Science **272**, 523 (1996).
[6] E. W. Wong, P. E. Sheehan, and C. M. Lieber, Science **277**, 1971 (1997).
[7] B. I. Yakobson and R. E. Smalley, Am. Sci. **85**, 324 (1997).
[8] P. Calvert, Nature (London) **399**, 210 (1999).
[9] P. M. Ajayan, Chem. Rev. **99**, 1787 (1999).
[10] Q. H. Wang *et al.*, Appl. Phys. Lett. **72**, 2912 (1998).
[11] R. Haggenmueller *et al.*, Chem. Phys. Lett. **330**, 219 (2000).
[12] Z. W. Pan *et al.*, Nature (London) **394**, 631 (1998).
[13] B. I. Yakobson, C. J. Brabec, and J. Bernholc, Phys. Rev. Lett. **76**, 2511 (1996).
[14] M. S. P. Shaffer and A. H. Windle, Macromolecules **32**, 6864 (1999), and references therein.
[15] V. Georgakilas *et al.*, J. Am. Chem. Soc. **124**, 760 (2002), and references therein.
[16] R. Andrews *et al.*, Chem. Phys. Lett. **303**, 467 (1999); **39**, 1681 (2001).
[17] The use of specific commercial materials does not imply endorsement of these products by NIST or the federal government.
[18] C. W. Peterson and B. W. Knight, J. Opt. Soc. Am. **63**, 1238 (1972).
[19] M. S. Dresselhaus, G. Dresselhaus, and P. C. Eklund, *Science of Fullerenes and Carbon Nanotubes* (Academic, New York, 1996).
[20] E. K. Hobbie and L. Sung, Am. J. Phys. **64**, 1298 (1996).
[21] S. Kim, J. Yu, and C. Han, Rev. Sci. Instrum. **67**, 3940 (1996).
[22] The expression $S(q_i) \approx S(0)\exp(-\xi_i^2 q_i^2/2) \propto 1 - \xi_i^2 q_i^2/2 + \ldots$ is motivated by a small-q expansion of the structure factors. These fits include a ''virtual'' background that is consistently larger than the measured scattering intensity in the high-q limit, suggesting that the effective background is weakly q dependent. The range of wave vector used in these fits is $q < 2\ \mu\mathrm{m}^{-1}$.
[23] G. B. Jeffery, Proc. R. Soc. London, Ser. A **102**, 161 (1922).
[24] B. J. Trevelyan and S. G. Mason, J. Colloid Sci. **6**, 354 (1951).
[25] E. J. Hinch and L. G. Leal, J. Fluid Mech. **52**, 683 (1972).
[26] O. L. Forgacs and S. G. Mason, J. Colloid Sci. **14**, 457 (1959).
[27] C. A. Stover, D. L. Koch, and C. Cohen, J. Fluid Mech. **238**, 277 (1992).
[28] M. Rahnama, D. L. Koch, and E. S. G. Shaqfeh, Phys. Fluids **7**, 487 (1995).
[29] E. Anczurowski and S. G. Mason, J. Colloid Interface Sci. **23**, 533 (1967).
[30] R. S. Stein and P. R. Wilson, J. Appl. Phys. **33**, 1914 (1962).
[31] Any free charge in the fullerene sheets will be mobile, and the polarizability parallel to the local symmetry axis of the tube is thus expected to be larger than that normal to this axis. The mean polarizability and anisotropy are defined as $\alpha = (\alpha_{\parallel} + 2\alpha_{\perp})/3$ and $\delta = (\alpha_{\parallel} - \alpha_{\perp})$, respectively, where $\alpha_{\parallel}$ and $\alpha_{\perp}$ denote the polarizabilty along directions parallel ($\parallel$) and perpendicular ($\perp$) to the tube backbone.
[32] The cartoon depicted in Fig. 1 suggests how the semiflexible nature of the tube shape might translate into an effectively larger tube width, or radius of gyration, which for the sake of simplicity we have crudely described here with a 2D model of high-aspect-ratio rectangles in the $x-z$ plane.